Journal of Materials Chemistry C

ROYAL SOCIETY OF CHEMISTRY

PAPER

View Article Online
View Journal | View Issue



Cite this: J. Mater. Chem. C, 2024, 12, 10036

# How to tune luminescent Cu(I) complexes with strong donor carbenes towards TADF?†

Jasper Guhl, ‡[a] Dragana Sretenović, ‡[b] Philipp Schmeinck,[c] Suren Felekyan,[b] Ralf Kühnemuth,[b] Christian Ganter, *[c] Claus A. M. Seidel, *[b] Christel M. Marian *[a] and Markus Suta *[c]

Cu(I) carbene complexes are common emitters of current emerging interest for next-generation OLED technology based on their encountered thermally activated delayed fluorescence (TADF) properties. However, general molecular design principles for successfully observable TADF properties of such complexes usually rely on π-acidic N-heterocyclic carbene (NHC) ligands, while Cu(I) carbene complexes with purely σ-donating NHC ligands are still scarce. Based on a simple synthetic approach reported by us earlier that offers large-scale access to this class of Cu(I) carbene complexes, we aim to elucidate design principles to enhance their TADF properties. In this work, we combined temperature-dependent time-resolved luminescence spectroscopy on different time scales (ns, μs, ms) with high-level DFT/MRCI calculations on a number of representative Cu(I) NHC complexes with the anionic carbene An6DAC and additional pyridine-derived ligands. Good agreement between experiment and theory related to the electronic nature of the optical transitions, the energy levels of the electronic states and the kinetics of interconversion controlled by the respective energy gaps was found. We conclude that both the electron-rich or electron-poor nature of the pyridine ligands and the coordination geometry (linear, trigonal planar) play a significant role in the outcome of the optical properties of these complexes. While electron-rich pyridine moieties induce decoupled prompt fluorescence and phosphorescence with connected low photoluminescence quantum yields, electron-poor pyridine moieties enhance a "push–pull" effect mediated by Cu(I) that favours TADF properties so that the luminescence intensity is increased by 1–2 orders of magnitude if the complex is trigonal. In the trigonal formyl pyridine complex, theory predicts high MLCT contributions to the electronic wavefunctions, so that the $T_1$ states should exhibit large spin–orbit coupling matrix elements (SOCMEs) with several excited singlet states. Indeed, in temperature dependent luminescence measurements, the electronic states behave as an intimately coupled ensemble. At 270 K, 56% of its luminescence can be attributed to TADF. However, while the luminescence of the trigonal complexes is brighter, their chemical Cu–pyridine bond is more labile. Overall, this study provides a detailed overview of the possibilities of targeted molecular design to selectively address desirable optical properties in organometallic compounds for potential applications in lighting.



Received 11th April 2024,
Accepted 14th June 2024

DOI: 10.1039/d4tc01487a

rsc.li/materials-c

## Introduction

Since the pioneering work of Tang *et al.*[1] on organic electroluminescent diodes in the 1980s, we have witnessed the evolution of four generations of small-molecule organic light-emitting diodes (OLEDs).[2–5] Currently, there is still no end of this evolution in sight: the first generation was based on fluorescent emitters and can therefore exploit at most 25% of the electrically generated excitons. The second generation made use of heavy-metal complexes based on, *e.g.*, Ir(III) or Pt(II) that enhance spin–orbit coupling by the heavy-atom effect and thus, lead to dominant phosphorescence. Due to ultrafast intersystem crossing from the excited singlet state to the triplet

[a] Institute for Theoretical and Computational Chemistry, Faculty of Mathematics and Natural Sciences, Heinrich Heine University Düsseldorf, 40225 Düsseldorf, Germany. E-mail: christel.marian@hhu.de
[b] Institute for Molecular Physical Chemistry, Faculty of Mathematics and Natural Sciences, Heinrich Heine University Düsseldorf, 40225 Düsseldorf, Germany. E-mail: claus.seidel@hhu.de
[c] Institute for Inorganic and Structural Chemistry, Faculty of Mathematics and Natural Sciences, Heinrich Heine University Düsseldorf, 40225 Düsseldorf, Germany. E-mail: christian.ganter@hhu.de

† Electronic supplementary information (ESI) available. See DOI: https://doi.org/10.1039/d4tc01487a

‡ These authors contributed equally.

manifold, this approach harvests both singlet and triplet excitons and increased the theoretically expected internal quantum efficiency of electroluminescence (IQE) to 100%. The third (exploiting thermally activated delayed fluorescence, TADF) and fourth (hyperfluorescence, combination of a TADF emitter with a narrow-band emitting fluorescent emitter) generations use less expensive materials and can in principle achieve 100% IQE as well. Despite those promising features, there are still several shortcomings to be tackled. With typical electroluminescence decay times in the microsecond regime, phosphorescent OLEDs (PhOLEDs) and OLEDs based on TADF are prone to photochemical side reactions in the excited state, which are detrimental to the operational durability of the device.[6] In particular, blue light emitting OLEDs are known to suffer from degradation of the emitter material.[7] TADF emitters have the advantage over PhOLED emitters that their synthesis does not rely on any precious heavy metals but are composed of earth-abundant elements and thus, less expensive. Besides purely organic donor–acceptor systems, complexes of the coinage metals, in particular Cu(I), have been used.[8–10] The preference for $d^{10}$ elements in TADF emitting transition metal complexes is related to the lack of energetically accessible metal-centered (MC) d → d* excitations that are known to cause predissociation of metal–ligand bonds in phosphorescent Ir(III) and Pt(II) complexes,[11] for example.

The energetic proximity of metal-to-ligand charge transfer (MLCT), ligand-to-ligand charge-transfer (LLCT) and ligand-centered (LC) excitations in Cu(I) complexes is both bless and curse—a bless because it forms the basis for a rich photochemistry and photophysics,[10] and a curse because low-lying $^3$LC states tend to act as dark traps for the excited state population with the tendency for non-radiative relaxation.[12,13] Dependent on the particular case, the population of MLCT states can be advantageous or disadvantageous for the luminescence properties of Cu(I) complexes involving triplet states. On the one hand, the hole in the Cu d shell enhances spin–orbit coupling (SOC) and thus increases the probability of intersystem crossing (ISC) and reverse ISC (rISC) processes that are necessary for harvesting the triplet excitons in OLEDs.[10,14,15] On the other hand, the pseudo Jahn–Teller effect on the $d^9$ electronic structure in an MLCT state causes large geometrical displacements which can be detrimental to the electro- or photoluminescence quantum yields ($\Phi_{EL}$ or $\Phi_{PL}$) of MLCT states and requires chemical ligand design strategies to sterically limit the distortion in the excited state.[16–23] In cationic Cu(I) complexes carrying an N-heterocyclic carbene (NHC) and an aromatic ligand, moreover the torsional orientation of the carbene and π-systems has an impact on the S–T energy gap, $\Delta E_{ST}$, and hence, the ability of these complexes to show phosphorescence or TADF.[24,25] Generally, $\Delta E_{ST}$ tends to be larger for MLCT states than for LLCT states.[19] For this reason, two-fold coordinated linear Cu(I) complexes with MLCT-type $S_1$ and $T_1$ states are often phosphorescent, whereas complexes with energetically low-lying LLCT states are more promising candidates for TADF if admixture of energetically close MLCT states is possible.

Among the linear coinage metal complexes, carbene metal amides stand out: depending on the π-acceptor strength of the carbene, the color of the LLCT emission can be tuned from blue to the NIR region and many of these complexes are TADF-active with high luminescence quantum yields.[21–23,25–32] Their ISC and rISC mechanism have been studied in great detail revealing solvent reorganization as well as vibronic coupling effects.[19,33–37] The direction of the CT is less obvious in cationic linear carbene Cu(I) complexes incorporating neutral aromatic imine ligands instead of an amide. Here, the carbene as well as the imine may adopt the role of the acceptor. Studies employing classical NHC and pyridine-based ligands revealed that the steric demand of the NHC and the presence of electron-withdrawing substituents in *para*-position of the pyridine ligand are important factors favoring luminescence involving the triplet state either directly or *via* TADF.[12,38]

Another class of efficient OLED emitters are zwitterionic mixed carbene coinage metal complexes combining an anionic malonate-derived NHC unit and a classical neutral NHC. Such complexes were reported to show bluish-white phosphorescence.[39] The overall charge neutrality of this class of compounds is advantageous for the fabrication of OLED devices due to their appreciable vapor pressure. Zwitterionic carbene Cu(I) units may alternatively be combined with neutral pyridine-based ligands and are also overall charge neutral. Specifically, in a recent paper we reported on a series of such complexes, comprising, *inter alia*, the linear derivatives **2a,b** and the trigonal compounds **3a,b** (Chart 1). In the present contribution we analyse the photophysical properties of these four complexes in depth with both, experimental and theoretical methods. The aim was to eventually establish a design principle for efficient TADF performance. Preliminary scans of the energy level scheme by quantum chemistry (Fig. 1) revealed that the acceptor properties of pyridine are insufficient for making the carbene-to-pyridine LLCT states the lowest singlet and triplet excited states.[40] In the linear complex with unsubstituted pyridine, $S_1$ and $T_1$ arise predominantly from local

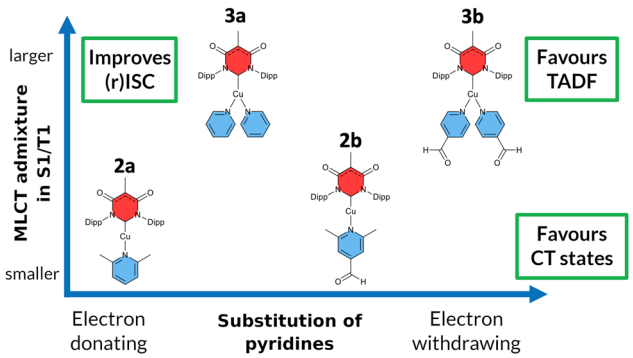


Chart 1 Overview of the different Cu(I) carbene complexes with electron-donating carbene (red) and pyridine ligands (blue) investigated within this work. The complexes are arranged in a 2-dimensional array based on the electron-withdrawing character of the pyridine moiety (abscissa) and the admixture of metal-to-ligand charge transfer character to the excited states (ordinate). Complexes in the top right corner are qualitatively expected to show prominent TADF properties.

excitations on the carbene ligand. With a $\Delta E_{ST}$ value of 0.394 eV, the singlet–triplet energy gap is too large enabling TADF at room temperature. Test calculations suggest that fluorination is not sufficient to increase the acceptor strength of the pyridine ligand, as F exerts a +M (mesomeric) effect in addition to a −I (inductive) effect. Possible substituents combining −I with −M effects are nitrile and formyl groups. Previous work on related cationic carbene pyridine Cu(I) complexes revealed, however, that a nitrile functionality in *para*-position of the pyridine ligand tends to coordinate to a Cu atom of a neighbouring linear complex, thus forming a coordination polymer.[38] When a formyl group was employed as an electron-withdrawing substituent instead, this complication did not arise. In the present case, $S_1$ and $T_1$ adopt LLCT character if 4-formylpyridine is used as a ligand in the neutral linear copper carbene complex which reduces $\Delta E_{ST}$ to merely 0.092 eV (Fig. 1). Moreover, MLCT states are found energetically close-by, thus promoting SOC. Thus, this linear 4-formylpyridine Cu(I) complex with an anionic donor carbene could be considered an ideal candidate for an efficient TADF emitter if it were not for the known problem that sterically unprotected electron-deficient Cu centers are susceptible to bond formation with additional coordinating molecules.[12,25,26,41,42] To prevent the accidental formation of trigonal complexes, we introduced methyl groups in *ortho*-position of the pyridine ring which increase the steric demand of the ligand, yielding the linear lutidine and 4-formyllutidine complexes **2a** and **2b**, respectively.[43] An alternative approach to increase the "pull" effect is the introduction of a second acceptor ligand resulting in the bis(formylpyridine) complex **3b**, for which lower energies of the LLCT and MLCT states in comparison to the LC states are calculated (Fig. 1). For the reasons outlined above, the four complexes **2a,b** and **3a,b** (Chart 1) were selected for our in-depth analysis of the photophysical properties.

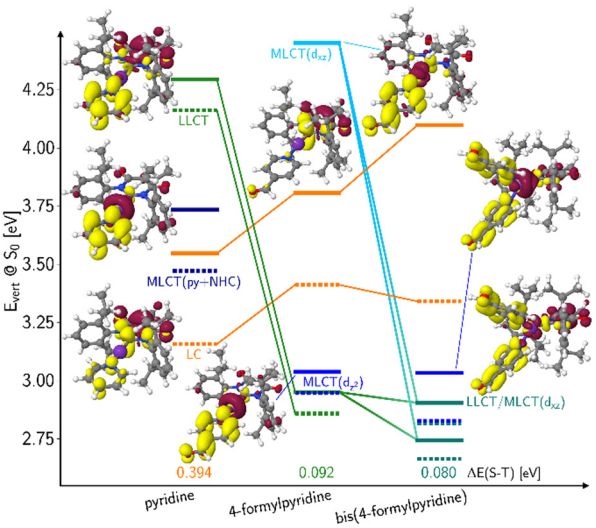


Fig. 1 DFT/MRCI energy level scan of the linear complexes with a pyridine or 4-formylpyridine ligand, respectively, and the bis(4-formylpyridine) complex **3b** at the ground-state geometry in dichloromethane solution and assignment of the electronic structures of the excited states. Solid lines represent singlet states, dashed lines triplets. Excitations are characterised by difference density plots (isovalue ±0.002). A loss of electron density with respect to the electronic ground state is shown in red, a gain in yellow.

According to the previously indicated guidelines, TADF is thus expectedly most prominent in a Cu(I) carbene complex with an electron-donating carbene and two strongly electron-withdrawing pyridine moieties to stabilize excited states with a strong LLCT character mediated by the redox-active Cu(I) central atom. In addition, a trigonal coordination pattern leads to an admixture of LLCT and MLCT character in the lowest electronically excited singlet and triplet states, resulting in larger mutual SOC compared to the respective linear complex (Fig. 1). These simple guidelines imply that the trigonal planar complex **3b** (Chart 1) should be a promising candidate for TADF in this uncommon scheme exploiting an electron-rich NHC ligand. In contrast, the linearly coordinated heteroleptic Cu(I) carbene complex **2a** should expectedly show prominent phosphorescence. It is the purpose of this work to combine advanced quantum chemical methods with time-resolved spectroscopy in suspensions of microcrystallites and the solid state in a temperature range between 10 K and 298 K to investigate whether these simple guidelines hold in practice to offer a possibility for targeted design of TADF emitters based on Cu(I) carbene complexes with strong donor carbenes. Due to chemical lability of the complexes in solution, the spectroscopy was carried out in cyclohexane suspensions of microcrystalline compounds. This method allowed for the preparation of sufficiently stable solid-state samples in standard cuvettes, thereby enabling absorption experiments, among other benefits. The validity of the collected data is supported by selected experiments on the neat powdered samples (see ESI,† Fig. S3).

Our synthesis started from the recently described moisture and air-stable one-dimensional coordination polymer **[Cu(An6DAC)]$_n$** which, upon treatment with the appropriate pyridine ligand, provided the respective linear or trigonal complexes, dependent on the particular substitution pattern of the pyridine derivative (Chart 1).[43] In addition to structural characterization of the synthesized compounds, excitation, absorption and steady-state emission spectra of four luminescent complexes were presented in that work, but the electronic nature of the emitting states, and their time-resolved luminescence properties with the corresponding temperature dependence had not yet been determined. This work is organized in a way that each complex is investigated in detail with respect to its energetic and dynamic properties. To characterize the relevant electronic states, we compared the experimental spectral properties with computed DFT/MRCI excited state energy levels. The coupling between those states was extracted from the temperature dependence of time-resolved luminescence data in distinct time regimes and thus obtained activation energies as well as rate constants are compared with the theoretically computed rate constants for emission and ISC. The results of each complex provide a reasonable data basis how structural design influences the optical properties in organometallic compounds (Chart 1). In this way, we demonstrate the possibilities and challenges of targeted molecular

 

design in selectively addressing desirable optical properties in organometallic compounds.

## Results and discussion

### The linear lutidine complex 2a

In this complex, a strongly σ-donating, anionic electron-rich carbene is combined with a relatively electron-rich pyridine moiety. Consequently, CT-type emission is not readily expected in **2a** and the luminescence should be governed by ligand-centred (LC) states. The excitation and emission spectra of this complex in Fig. 2 confirm this idea. At the excitation wavelength of the luminescence experiments (375 nm), primarily the $S_1$ state is populated. The experimental optical steady-state spectroscopic parameters of all complexes in cyclohexane suspension at 298 K are compiled in Table 1. In addition, we analysed the time-resolved luminescence decays in distinct time regimes in a wide temperature range: nanoseconds to resolve prompt fluorescence, microseconds and milliseconds to characterize TADF and phosphorescence. Often, the decays were multi-exponential so that we listed the intensity-averaged luminescence lifetime, $\langle\tau\rangle_I$, of all complexes in Table 2 and the individual parameters of all components in Tables S1–S11 (ESI†). Our quantum chemical calculations indicate that its wavefunction is dominated by a $^1$LC(carbene) character with small $^1$LLCT(carbene-to-lutidine) contributions (vertical excitation wavelength 349 nm, oscillator strength $f$ = 0.093). Below $S_1$, the corresponding $^3$LC(carbene) and a $^3$MLCT($d_{z^2}$-to-lutidine) state are found in the vertical energy spectrum, respectively. The latter state is practically degenerate with $S_1$ in the Franck–Condon (FC) region, but does not play an essential role in the emission process. Occupation of the C–N-antibonding π* orbital in the $S_1$ state leads to a substantial elongation of the carbene C–N bonds which stabilizes the LC(carbene) contributions to the $S_1$ wavefunction. Blue emission with a maximum at $\lambda_{max} \approx 450$ nm is observed in the luminescence spectrum at room temperature. The excitation and emission spectra of the powdered samples are in excellent agreement with those measured in cyclohexane suspension (Fig. 2A). However, the measured excitation spectrum in cyclohexane suspension does not completely overlap with the absorption spectrum (Fig. 2B). This discrepancy is quantified by the ratio of excitation and absorption values, normalized at the excitation wavelength of 375 nm (Fig. 2B top). The normalized excitation/absorbance ratio at longer wavelengths indicates the presence of additional non-luminescent species in suspensions (Fig. 2). Despite the observed discrepancy, the theoretically predicted spectrum agrees well with the longest excitation band.

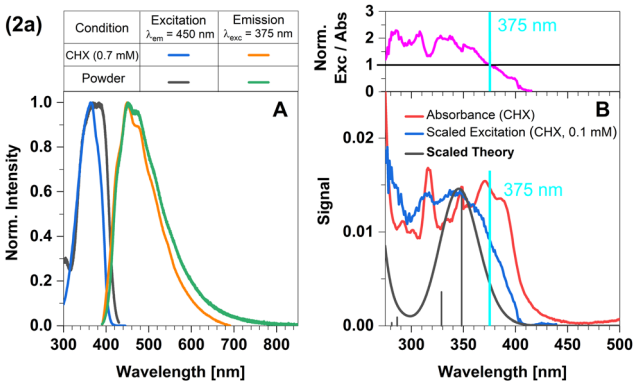


Fig. 2 Spectra of compound **2a** at 298 K (summary in Table 1). The measurements procedures are described in detail in Experimental and theoretical procedures. (A) Excitation and emission spectra in liquid cyclohexane (CHX) and powder. (B) For a qualitative comparison of the absorption properties, the excitation and the broadened DFT/MRCI spectrum were scaled to the experimental absorbance spectrum, which was corrected for baseline and scattering (eqn (3)).

Despite a mutual spin–orbit coupling matrix element (SOCME) below 1 cm$^{-1}$ and an adiabatic $S_1$–$T_1$ energy separation $\Delta E_{ST,adiab} \approx 0.65$ eV, theoretically expected $S_1$–$T_1$ ISC appears to be competitive to prompt fluorescence (Table 3) and gives rise to a weak portion of phosphorescence. Time-resolved measurements of **2a** in cyclohexane suspension were performed at four different temperatures (10, 60, 160, and 260 K) (Fig. 3) to verify this kinetic scheme experimentally. The measured intensity-averaged decay time $\langle\tau_{ns}\rangle_I$ of prompt fluorescence in the nanosecond regime agrees well with the estimate for the upper limit of the fluorescence lifetime of state (I), $\tau^{(I)}_{PF,lim}$ (Table 3), considering only $k_F$ and $k_{ISC}$. Thus, internal conversion (IC) is not a main modulator of the fluorescence properties, which holds true for most of the other compounds with the exception of **2b**. From the resulting decay times and amplitudes, intensity-weighted averages, $\langle\tau_{ns}\rangle_I$, have been generated. Their temperature dependence was approximated by a simple exponential behavior with temperature-independent activation energy $E_A$ and rate constants $k_A$ and $k_S$ [eqn (1)].

$$\langle\tau_{ns}\rangle_I(T) = \left(k_S + k_A \cdot \exp\left(-\frac{E_A}{k_B T}\right)\right)^{-1} \quad (1)$$

Possible temperature-dependent processes affecting singlet state lifetimes are internal conversion, intersystem crossing, diffusion-controlled quenching *etc.*, but for the studied samples the assumption of one process was sufficient to fit the data within the experimental noise level (Fig. 3B). Fit results of all compounds in the nanosecond range are given in Table S12 (ESI†).

The computed vertical emission wavelength at the $S_1$ minimum (443 nm) is also in good agreement with the experimental observations ($\lambda_{max} \approx 450$ nm). The vibronic progression frequency ($\Delta\tilde{\nu} \approx 1350$ cm$^{-1}$), observable in the emission spectrum of powdered **2a** at 77 K (see Fig. S3, ESI†), is compatible with the coupling of the electronic transition to a C–N stretching vibration of the carbene moiety and indicates luminescence from a LC state. Due to the large $S_1$–$T_1$ energy gap of $\Delta E_{ST} \approx 0.64$ eV, delayed fluorescence is not detected in this compound within the regarded temperature range. The observed phosphorescence in the millisecond time regime (see Table S2, ESI†) is in line with the LC nature of the $T_1$ excitation, associated with a low radiative rate constant (calculated value $k_P \approx 10^1$ s$^{-1}$).

Table 1 Experimental steady-state spectroscopic parameters of complexes **2a**, **2b**, **3a** and **3b**, powdered and in liquid cyclohexane suspension at 298 K. The tables include excitation ($\lambda_{exc,m}$) and emission maxima ($\lambda_{em,m}$), apparent Stokes shifts ($\Delta\tilde{\nu}_s$), 0–0 energies ($\tilde{\nu}_{00}$) and emission band full widths at half maximum (FWHM emission), and normalized photoluminescence quantum yields ($\Phi_{PL}^{norm}$) computed by normalization of the respective signals to the signal of compound **3b**

| | Compound **2a** | | Compound **3a** | | Compound **2b** | | Compound **3b** | |
|---|---|---|---|---|---|---|---|---|
| Parameter at condition | Powder | Cyclohexane | Powder | Cyclohexane | Powder | Cyclohexane | Powder | Cyclohexane |
| $\lambda_{exc,m}$ [nm] | 369 | 363 | 364 | 368 | 407 | 386 | 490 | 395 |
| $\lambda_{em,m}$ [nm] | 451 | 449 | 504 | 502 | 527 | 521 | 591 | 590 |
| $\Delta\tilde{\nu}_s$ [cm$^{-1}$] | 4615 | 5001 | 7605 | 7450 | 4170 | 4122 | 3400 | 3800 |
| $\tilde{\nu}_{00}$ [cm$^{-1}$] | 23 987 | 24 938 | 23 403 | 24 570 | 20 786 | 21 692 | 18 477 | 19 493 |
| FWHM emission [cm$^{-1}$] | 7040 | 5651 | 5937 | 5240 | 5799 | 4687 | 3945 | 3607 |
| $\Phi_{PL}^{norm}$ ($\lambda_{exc}$ = 375 nm) | — | 0.08 | — | 0.01 | — | 0.02 | — | 1.00 |

Table 2 Experimental time-resolved luminescence decay parameter (intensity-averaged luminescence lifetime $\langle\tau\rangle_I$) of complexes **2a**, **2b**, **3a** and **3b**, powdered (298 K and 80 K) and in frozen cyclohexane suspension at 260 K and 60 K (see Methods). All decays are multi-exponential, individual decay times and species fractions are provided in the ESI (see Tables S1–S8, ESI). No em.: no decay component in this time range

Powder

| | Compound **2a** | | Compound **3a** | | Compound **2b** | | Compound **3b** | |
|---|---|---|---|---|---|---|---|---|
| Parameter at $T$ [K] | 298 | 80 | 298 | 80 | 298 | 80 | 298 | 80 |
| $\langle\tau_{ns}\rangle_I$ [ns] | 1.7 | 5.9 | No em. | No em. | 3.5 | 22.3 | No em. | No em. |
| $\langle\tau_{\mu s}\rangle_I$ [μs] | No em. | No em. | No em. | No em. | 1.7 | No em. | 7.6 | 27.4 |
| $\langle\tau_{ms}\rangle_I$ [ms] | 1.2 | 2.2 | 0.4 | 1.3 | No em. | 0.04 | No em. | No em. |

Solid cyclohexane suspension

| Parameter at $T$ [K] | 260 | 60 | 260 | 60 | 260 | 60 | 260 | 60 |
|---|---|---|---|---|---|---|---|---|
| $\langle\tau_{ns}\rangle_I$ [ns] | 2.6[a] | 5.9[a] | 0.5[c] | 1.2[c] | 1.6[f] | 10.1[f] | 0.4[i] | 1.1[i] |
| $\langle\tau_{\mu s}\rangle_I$ [μs] | No em. | No em. | 338.0[d] | 208.6[d] | 55.4[g] | 267.3[g] | 10.0[j] | 28.3[j] |
| $\langle\tau_{ms}\rangle_I$ [ms] | 2.4[b] | 14.2[b] | 0.6[e] | 9.0[e] | 0.18[h] | 4.5[h] | No em.[k] | No em.[k] |

[a] See Table S1 (ESI). [b] See Table S2 (ESI). [c] See Table S3 (ESI). [d] See Table S4 (ESI). [e] See Table S5 (ESI) (for 260 K, within error the emission presumably is the same as in microseconds). [f] See Table S6 (ESI). [g] See Table S7 (ESI). [h] See Table S8 (ESI) (for 260 K, within error the emission presumably is the same as in microseconds). [i] See Table S9 (ESI). [j] See Table S10 (ESI). [k] The detected emission in the millisecond time range (see Table S11, ESI) does not originate from the compound, but from its free ligand (for more details, see chapter 5.2. of the ESI).

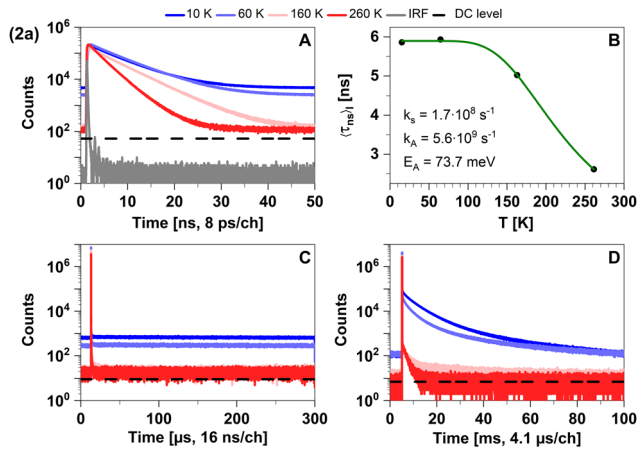


Fig. 3 Time-resolved luminescence measurements of compound **2a** in solid cyclohexane suspension at temperatures of 10 K, 60 K, 160 K, 260 K, in three distinct time regimes. (A) Decays in nanoseconds. (B) Temperature-dependence of the intensity-weighted prompt fluorescence lifetime $\langle\tau_{ns}\rangle_I$. The green line represents the fit of the experimental data according to eqn (1). All fit results with their respective errors are shown in Table S12 (ESI†). (C) Microseconds with no decay component. (D) Decays in milliseconds. All luminescence decays exhibit multi-exponential behaviour. The intensity-averaged luminescence lifetimes $\langle\tau\rangle_I$ are listed in Table 2, the individual decay times and species fractions are compiled in Tables S1 and S2 (ESI†). The excitation wavelength was at 375 nm, and the detection wavelength 460 nm. The counts that correspond to the dark count (DC) rate of the detector (95 Hz) are marked with a black dashed line.

As expected, phosphorescence becomes efficiently quenched at elevated temperatures (see Fig. 3D). Overall, the appearance of the photoluminescence spectra of the linear lutidine complex **2a** can be interpreted as conventional fluorescence and energetically separated weak phosphorescence. The photoluminescence properties of powdered **2a** agree very well with those measured in the cyclohexane suspension.

### The trigonal pyridine complex 3a

Like in complex **2a**, the strongly σ-donating carbene ligand is combined with two slightly electron-rich pyridine moieties. This design is also not expected to readily give rise to TADF but rather conventional decoupled fluorescence and phosphorescence. The trigonal coordination pattern should, however, effectively decrease the $S_1$–$T_1$ energy gap $\Delta E_{ST}$ and also the energies of the lowest excited states compared to the energies in **2a**. Previous experimental and quantum chemical studies on cationic NHC Cu(I) pyridine complexes[12,13] had shown that association of a second pyridine ligand shifted the relative energies of LC, LLCT and MLCT states such that trapping of the photoexcitation in a long-lived $^3$LC state was suppressed. This effect enhances the luminescence efficiency of the complexes. In the present case, trigonal complexes are formed as well when the sterically less demanding pyridine instead of

 

Table 3 Computed photophysical data of the complexes **2a**, **3b**, **3a**, **3b**

| Parameter | Compound **2a** | Compound **3a** | Compound **2b** | Compound **3b** |
|---|---|---|---|---|
| $\lambda_{abs}$ ($S_1$) [nm] | 349 (LC/LLCT) | 329 (LLCT/MLCT($d_{xz}$)) | 412 (LLCT) | 452 (LLCT/MLCT($d_{xz}$)) |
| $f_{abs}$ ($S_1$) | 0.09251 | 0.00916 | 0.03057 | 0.01507 |
| $\lambda_{em,vert}$ [a] [nm] | 443 ($^1$LC) [b]<br>664 ($^3$LC) | 606 ($^1$LC)<br>665 ($^3$LC) | 563 ($^1$LLCT)<br>591 ($^3$LLCT)<br>615 ($^3$LC) | 704 ($^1$LLCT)<br>728 ($^3$LLCT)<br>707 ($^1$MLCT)<br>748 ($^3$MLCT) |
| $k_F$ [$s^{-1}$] | $4.0 \times 10^7$ ($^1$LC) | $1.0 \times 10^7$ ($^1$LC) | $6.3 \times 10^6$ ($^1$LLCT) | $4.2 \times 10^5$ ($^1$LLCT)<br>$2.6 \times 10^6$ ($^1$MLCT) |
| $k_{ISC}$ (298 K) [$s^{-1}$] | $8.0 \times 10^7$ ($^1$LC–$^3$LC) | $1.5 \times 10^9$ ($^1$LC–$^3$LC) | $2.7 \times 10^6$ ($^1$LLCT–$^3$LLCT)<br>$8.5 \times 10^5$ ($^1$LLCT–$^3$LC) | $2.3 \times 10^7$ ($^1$LLCT–$^3$LLCT)<br>$9.1 \times 10^{10}$ ($^1$LLCT–$^3$MLCT)<br>$2.7 \times 10^{10}$ ($^1$MLCT–$^3$MLCT)<br>$2.8 \times 10^{11}$ ($^1$MLCT–$^3$LLCT) |
| $\tau^{(i)}_{PF,lim}$ (298 K) [ns] [c] | 8.3 | 0.7 | 101.5 | 0.010 ($^1$LLCT)<br>0.004 ($^1$MLCT) |
| $k_{rISC}$ (298 K) [$s^{-1}$] | — | $5.1 \times 10^{-2}$ ($^3$LC–$^1$LC) | $1.0 \times 10^5$ ($^3$LLCT–$^1$LLCT)<br>$1.8 \times 10^3$ ($^3$LC–$^1$LLCT) | $3.1 \times 10^5$ ($^3$LLCT–$^1$LLCT)<br>$2.1 \times 10^9$ ($^3$MLCT–$^3$LLCT)<br>$5.7 \times 10^8$ ($^3$MLCT–$^1$MLCT)<br>$2.4 \times 10^8$ ($^3$LLCT–$^1$MLCT) |
| $k_P$ (77 K) [$s^{-1}$] | $1.1 \times 10^1$ ($^3$LC) | $8.6 \times 10^1$ ($^3$LC) | $7.6 \times 10^1$ ($^3$LLCT)<br>$2.7 \times 10^1$ ($^3$LC) | $1.4 \times 10^4$ ($^3$LLCT)<br>$7.9 \times 10^3$ ($^3$MLCT) |
| $\Delta E_{ST,ad.}$ [eV] | 0.645 (LC) | 0.464 (LC) | 0.046 (LLCT)<br>−0.001 ($^1$LLCT–$^3$LC) | 0.058 (LLCT)<br>0.095 (MLCT) |

[a] Multiple entries indicate that more than one minimum was found on the $S_1$ or $T_1$ potential energy hypersurface, respectively. Adiabatic excitation energies and photophysical properties at these minima are given in the ESI. [b] The $^1$LC state was optimised with the constrained inter-ligand dihedral angle of the $^3$LC state. It does not constitute a proper minimum on the $S_1$ potential energy hypersurface. A proper minimum could not be obtained with the PBE0 functional. [c] Estimate for the upper limit of the fluorescence lifetime of state (i) with several ISC channels to $n$ triplet states: $\tau^{(i)}_{PF,lim} = 1 \Big/ \left(k^{(i)}_F + \sum_n k^{(i)}_{ISC,n}\right)$ based on the computed rate constants in this table. For this estimate, internal conversion is not considered.

2,6-lutidine is added to the zwitterionic NHC Cu(I) coordination polymer in excess.[43]

The agreement between cyclohexane and powder spectral data is quite good (Fig. 4A). Although the apparent absorbances of **2a** and **3a** (Fig. 2 and 4), measured in cyclohexane suspensions of microcrystallites, and their excitation spectra slightly differ, their excitation maxima at around 367 nm are similar (Table 1). Remarkably, the peak width of the first excitation band of **3a** is much narrower than the one of **2a**. Simultaneously, the emission maximum of **3a** is significantly red-shifted compared to that of **2a** (Fig. 4). Among the four complexes, **3a** exhibits the largest apparent Stokes shift of 7605 $cm^{-1}$.[43] Like in **2a**, a vibronic progression ($\Delta\tilde{\nu} \approx 1200$ $cm^{-1}$) is observable in the emission spectrum of the powder at 77 K[43] (Fig. S3, ESI†), which indicates an LC state as the emitting state.

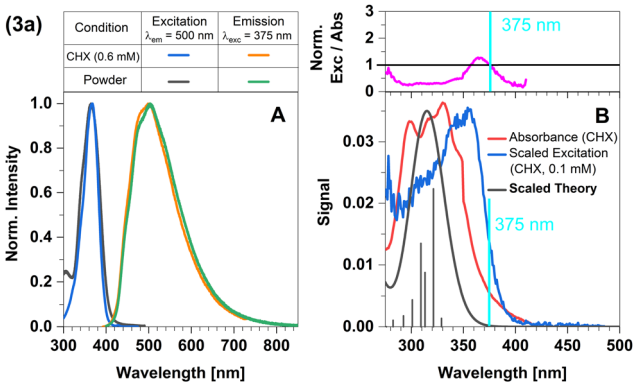


Fig. 4 Spectra of compound **3a** at 298 K (summary in Table 1). The measurements procedures are described in detail in Experimental and theoretical procedures. (A) Excitation and emission spectra in liquid cyclohexane (CHX) and powder. (B) For a qualitative comparison of the absorption properties, the excitation and the broadened DFT/MRCI spectrum were scaled to the experimental absorbance spectrum, which was corrected for baseline and scattering (eqn (3)).

The predicted theoretical spectrum is clearly blue-shifted compared to the absorption and excitation spectra in cyclohexane (Fig. 4B). The deviations are particularly pronounced around the excitation wavelength of 375 nm. A quantum chemical analysis of the vertical excitation energies and electronic structures of the low-lying singlet and excited states in the FC region[43] had shown that the LC(carbene) and MLCT($d_{z^2}$) dominated states of **3a** are blue shifted compared to their **2a** congeners whereas the states exhibiting mainly LLCT(NHC-to-pyridine) or MLCT($d_{xz}$) character are stabilized by the coordination of a second pyridine ligand. The $^1$LC state, which was primarily excited in **2a**, is hardly accessible in **3a** at the excitation wavelength ($\lambda_{ex}$ = 375 nm) used to record the

emission spectra. The lowest-lying excited singlet state rather possesses mixed $^1$LLCT and $^1$MLCT($d_{xz}$) character. The $^3$LC state is blue-shifted as well, but remains the lowest excited triplet state. Admixture of MLCT($d_{xz}$) contributions to the $T_1$ wave function causes an untypically large oscillator strength of the $T_1 \leftarrow S_0$ absorption. Due to the strong SOC between the Cu $d_{xz}$ and $d_{z^2}$ orbitals,[14] intensity is mainly borrowed from the spin-allowed $S_3 \leftarrow S_0$ transition exhibiting MLCT($d_{z^2}$) character (for details, see Table S32, ESI†). Therefore, theory suggests that the long wavelength tail of the excitation spectrum stems from the spin-forbidden $T_1$ absorption. This interpretation is in line with the observation that the origins of the excitation and phosphorescence emission spectra overlap (Fig. 4). According to the calculations, the emission of **3a** is thus expected to have a dominant character of phosphorescence. Another intriguing experimental observation is the large Stokes shift of the emission of **3a** (Fig. 4). Inspection of the energy schemes (Fig. S165, ESI†) reveals that the nuclear arrangement at the relaxed $T_1$ geometry of **3a** is very unfavourable for the $S_0$ state. The observed large Stokes shift is thus a consequence of the simultaneous lowering of the $T_1$ and steep rise of the $S_0$ state potential energies. The normalized excitation/absorbance ratio at shorter wavelengths indicates the presence of additional non-luminescent species in suspensions (Fig. 4).

Quickly decaying fluorescence was observed in our time-resolved spectroscopy experiments of **3a** in solid cyclohexane suspension alongside phosphorescence in the late microsecond and early millisecond time regime (Fig. 5).

This characterization agrees well with the time-resolved data in Tables 2 and 3. We attribute the apparent sub-nanosecond decay of the $S_1$ population to a competition between fluorescence and efficient ISC due to MLCT contributions to the singlet and triplet wavefunctions. This agrees with the estimated upper limit of the fluorescence lifetime $\tau_{PF,lim}^{(i)}$ (298 K) = 0.7 ns (see Table 3). The MLCT admixture is reduced upon geometry optimization of the $T_1$ state, resulting in a relatively low radiative rate constant (calculated value $k_P \approx 10^2\ s^{-1}$). This is compatible with measured phosphorescence decay times in the 100 μs–10 ms regime at $\Phi_{PL} \approx 2\%$.[43] Like in **2a**, the phosphorescence is efficiently thermally quenched by increasing temperature from 10 K to 260 K. Thus, the trigonally coordinated complex **3a** is dominated by phosphorescence from a $^3$LC state in the regarded temperature range based on an efficient ISC from the excited $S_1$ state.

### The linear formyl lutidine complex 2b

In order to favour TADF in the regarded Cu(I) complexes, electron-withdrawing lutidine or pyridine ligands are necessary that stabilize LLCT-type instead of LC states. For this purpose, we now consider a modified version of **2a** with an electron-withdrawing formyl substituent in *para* position of the lutidine ligand that gives rise to the linear Cu(I) complex **2b**. Moreover, the steric bulk of the methyl groups in *ortho* position limits the torsional flexibility in the formyl lutidine complex **2b**. Considering the isolated complex, we only found one stable conformer with a ligand twist angle of approx. 26° in the electronic ground

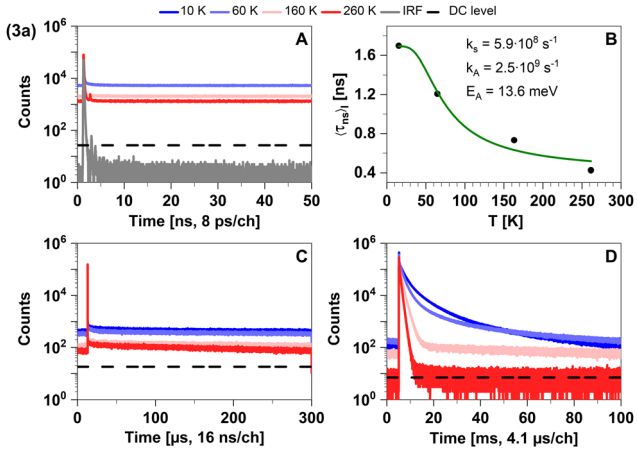


Fig. 5 Time-resolved luminescence measurements of compound **3a** in solid cyclohexane suspension at temperatures of 10 K, 60 K, 160 K, 260 K, in three distinct time regimes. (A) Decays in nanoseconds. (B). Temperature-dependence of the intensity-weighted prompt fluorescence lifetime $\langle\tau_{ns}\rangle_I$. The green line represents the fit of the experimental data according to eqn (1). All fit results with their respective errors are shown in Table S12 (ESI†). (C) Decays in microseconds. (D) Decays in milliseconds. All luminescence decays exhibit multi-exponential behaviour. The intensity-averaged luminescence lifetimes $\langle\tau\rangle_I$ are listed in Table 2, the individual decay times and species fractions are compiled in Tables S3–S5 (ESI†). The excitation wavelength was at 375 nm, and the detection wavelength 495 nm. The counts that correspond to the dark count (DC) rate of the detector (95 Hz) are marked with a black dashed line.

state in the calculations, compared to about 10° in a crystalline environment as determined by X-ray diffraction.[43] According to our quantum chemical studies, the ligand twist angles at the excited-state minima range from about 20° for the lowest LLCT(NHC-to-formyl lutidine) states over 23° in the $^3$LC(formyl lutidine n$\pi^*$) and 31° in the LC (NHC) to about 51° in the MLCT($d_{z^2}$-to-formyl lutidine) states. As intended, the S–T energy gaps of the LLCT and MLCT states are much smaller than for the LC(NHC) state (Fig. 6).

Excitation with a wavelength of 375 nm (approx. 3.3 eV) addresses a mixture of LLCT and MLCT states which are energetically close at the ground-state geometry (Fig. 6). The $^1$LLCT state exhibits higher absorbance than $^1$MLCT and is therefore preferentially populated. The $^1$LC(NHC) state lies energetically much higher in the FC region and cannot be reached with the chosen excitation wavelength. The LLCT, LC (NHC) and MLCT($d_{z^2}$) states of **2b** form minima on the $S_1$ or $T_1$ potential energy surfaces, respectively (Fig. 6). The barrier separating the MLCT minima from the lower-lying LLCT minima is estimated to be 12 meV (see Fig. S164, ESI†) and hence easily overcome. Direct emission from the MLCT minima is therefore not likely to occur in this complex.

Quantum chemistry predicts larger displacements of the nuclear coordinates between the minimum structures of the $^3$LC and $^3$LLCT states, which are adiabatically nearly degenerate (Fig. 6). The $^3$LC(NHC) state is long-lived as the equilibration with the other triplet potential wells is kinetically hindered by high reorganization energies. Their populations are

 

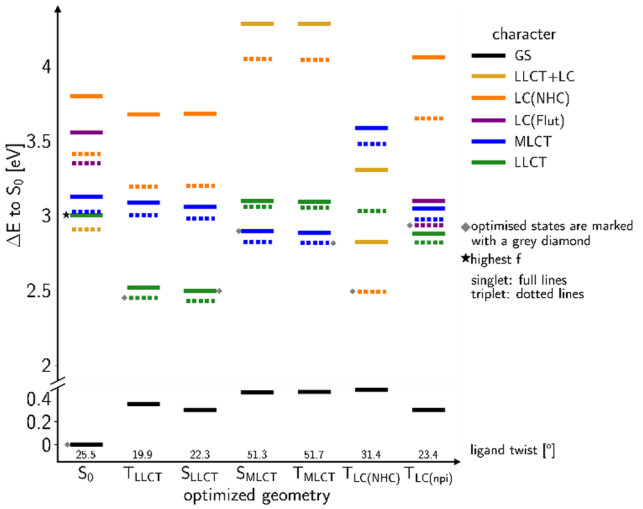


Fig. 6 Overview over the computed vertical DFT/MRCI energy levels at optimized geometries of low-lying states of complex **2b**. The $S_0$ energy at the optimized ground-state geometry serves as common energy offset.

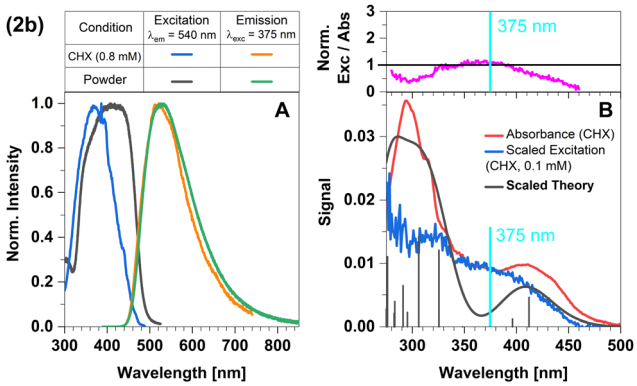


Fig. 7 Spectra of compound **2b** at 298 K (summary in Table 1). The measurements procedures are described in detail in Experimental and theoretical procedures. (A) Excitation and emission spectra in liquid cyclohexane (CHX) and powder. (B) For a qualitative comparison of the absorption properties, the excitation and the broadened DFT/MRCI spectrum were scaled to the experimental absorbance spectrum, which was corrected for baseline and scattering (eqn (3)).

interconvertible at room temperature, but a small portion appears to get trapped in the $^3$LC potential well at lower temperatures and decays *via* $^3$LC phosphorescence. These findings match the experimentally recorded low $\Phi_{PL} \approx 1\%$.[43]

The broad and structureless emission band (Fig. 7A) matches the predicted LLCT character of the emissive state. The absorption spectrum agrees well with that from theory (Fig. 7B). The normalized excitation/absorbance ratio at shorter wavelengths indicates small contributions of additional non-luminescent species in suspensions (Fig. 7 and 4).

Vibronic coupling between the MLCT and LLCT states is expected to enhance the ISC and rISC between the $^1$LLCT and $^3$LLCT states. The small $\Delta E_{ST}$ value of the LLCT states and the admixture of small amounts of MLCT($d_{xz}$) character (Fig. S116 and S124, ESI†) suggest that thermally activated up-conversion to the corresponding singlet potential well is possible. Thus, we expect a multiexponential luminescence decay.

In the temperature range from 270 K to 100 K, the mean emission position red-shifts as phosphorescence takes over. However, as the temperature decreases below 100 K, we observe the opposite trend and the emission maximum shifts to shorter wavelengths (Fig. 8A). This probably occurs due to dissociation of small portions of the sample and consequent emission of the free ligand (4-formyl-2,6-lutidine). The spectrum of the free ligand was compared with the spectrum of the sample at 10 K (Fig. 8B).

In time-resolved measurements within the nanosecond time regime, we observe a significant increase of the offset fraction upon cooling. This observation implies slowly decaying emissive states at all temperatures (Fig. 9A). The temperature dependence of the slow components does not follow a simple single barrier model anymore as implied by eqn (1). To include the predicted fast equilibration of the LLCT and MLCT populations, we fitted the temperature-dependent behaviour of the delayed luminescence decay times to the following equation assuming Boltzmann thermalization among the involved states:

$$\langle\tau\rangle(T) = \frac{2 + \exp\left(-\frac{E_1}{k_B T}\right) + 3\exp\left(-\frac{E_2}{k_B T}\right) + \exp\left(-\frac{E_3}{k_B T}\right) + \exp\left(-\frac{E_4}{k_B T}\right)}{2k_0 + k_1\exp\left(-\frac{E_1}{k_B T}\right) + 3k_2\exp\left(-\frac{E_2}{k_B T}\right) + k_3\exp\left(-\frac{E_3}{k_B T}\right) + k_4\exp\left(-\frac{E_4}{k_B T}\right)} \quad (2)$$

where the factors 2 and 3 account the state degeneracies of the triplet sublevels. $k_0$ and $k_1$ refer to the $T_1$ state, split by $E_1$, while $k_2$ and $E_2$ represent $T_2$. $k_3(E_3)$ and $k_4(E_4)$ are rate constants (energies) associated with the singlet states $S_1$ and $S_2$, respectively. For details, see section Experimental and theoretical procedures.

To further investigate the TADF properties, we measured time-resolved emission spectra (TRES) at 270 K, 220 K, 180 K, and 10 K (Fig. 10A–D). At the highest temperature (270 K), we observed that the spectra in the nanosecond and microsecond time regimes strongly overlap which can be attributed to the simultaneous presence of TADF and phosphorescence. As **2b** is cooled down, the spectral overlap decreases and two separate emission bands can be resolved. The emission in the nanosecond time regime exhibits a blue shift from 535 nm to 520 nm, while the emission in the microsecond time regime shifts towards longer wavelengths and even overlaps with the emission in milliseconds. Furthermore, the emission in both the microsecond and millisecond time regimes feature vibronic fine structure at low temperatures, which is typical for LC-related emission. In contrast, the emission band in the ns time range is broad and barely shows any fine structure implying emission from CT-type states. This observation suggests that

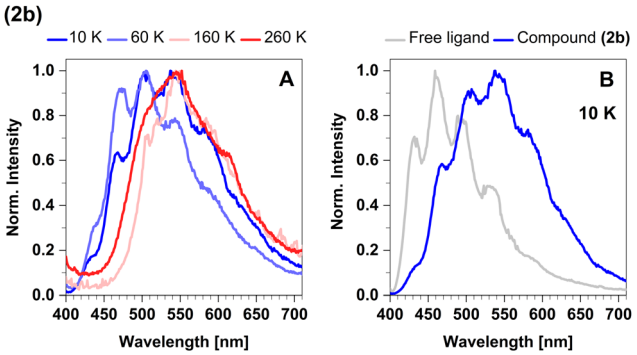


Fig. 8 (A) Steady-state luminescence spectra of **2b** in cyclohexane suspension at selected temperatures of 10 K, 60 K, 160 K, and 260 K. (B) Comparison of the steady-state spectrum of **2b** with the free ligand spectrum obtained in cyclohexane solution at 10 K. The excitation wavelength was 375 nm.

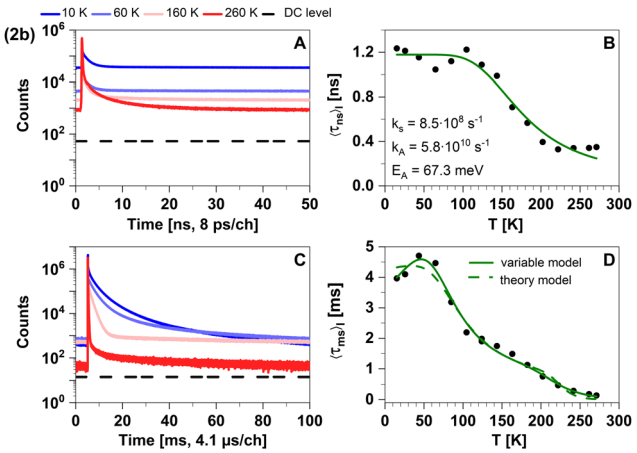


Fig. 9 Time-resolved luminescence measurements of compound **2b** in solid cyclohexane suspension at selected temperatures of 10 K, 60 K, 160 K, 260 K, in two distinct time regimes. Related decay components recorded in the temperature range from 10 K to 270 K are provided in Fig. S4 (ESI†). The excitation wavelength was 375 nm, and the detection emission wavelength 540 nm. (A) Decay curves in nanoseconds. (B) Temperature dependence of the intensity-weighted prompt fluorescence lifetime $\langle\tau_{ns}\rangle_I$. The green line represents the fit of the experimental data according to eqn (1). All fit results with their respective errors are shown in Table S12 (ESI†). (C) Decays in milliseconds. (D) Temperature-dependence of the intensity-weighted luminescence lifetime $\langle\tau_{ms}\rangle_I$ with all parameters compiled in Tables S13 and S14 (ESI†). The green lines represent least-squares fits of eqn (2) to the experimental data. Solid line (variable model, Table S13, ESI†): $E_1$ and $E_4$ are free parameters while $E_2$ and $E_3$ are fixed to theoretically computed zero-point vibrational energy corrected adiabatic values of 28.5 meV and 52.2 meV, respectively. Dashed line (theory model, Table S14, ESI†): all energies are fixed to theoretically computed zero-point vibrational energy corrected adiabatic values (Table S15, ESI†). The intensity-averaged luminescence lifetimes $\langle\tau_{\mu s}\rangle_I$ are listed in Table 2, the individual decay times and species fractions are compiled in Tables S6–S8 (ESI†). The counts that correspond to the dark count (DC) rate of the detector (95 Hz) are marked with a black dashed line.

phosphorescence from a $^3$LC state is involved in the microsecond time range and becomes the dominant process at lower temperatures. Luminescence within the millisecond time range

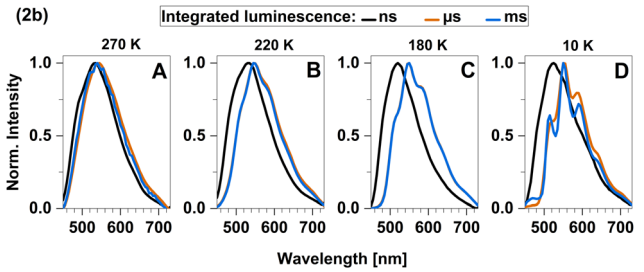


Fig. 10 Time-resolved emission spectra (TRES) of **2b** in solid cyclohexane suspension obtained at four different temperatures: (A) 270 K, (B) 220 K, (C) 180 K and (D) 10 K.

displays intricate multi-exponential characteristics (Fig. S8, ESI†). Upon careful spectral analysis, we deduced that the predominant source of luminescence arises from compound **2b**, with a minor contribution originating from leached ligand (Fig. S10, ESI†).

In the temperature range from 100 K to 270 K, we observed a non-linear dependence of the logarithmic rate constant on the reciprocal temperature, which is indicative for limited thermal coupling in that temperature range. This implies that the rISC rate of **2b** cannot compete with the decay rate of $T_1$ in that temperature range yet and thus, must be at most of similar order of magnitude of $k_P$. It also matches the fact that phosphorescence can be experimentally distinguished from fluorescence at low temperatures while TADF only becomes relevant at temperatures above 220 K. Overall, TADF in **2b** is based on ISC and rISC between $^1$LLCT and $^3$LLCT states that admix with MLCT states. Additionally, the quasi-degeneracy between the $^3$LLCT and a $^3$LC state (Fig. 6) leads to the observation of phosphorescence with vibronic fine structure at low temperatures ($T < 200$ K, Fig. 10).

### The trigonal formyl pyridine complex 3b

Replacement of the pyridine ligands in **3a** with the electron-withdrawing 4-formylpyridine results in complex **3b**. Similarly to **2b**, this leads to an energetic stabilization of the LLCT and MLCT($d_{z^2}$) states, with the easier accessibility of MLCT($d_{xz}$) states caused by the energetic increase of the corresponding ligand-field orbital due to the trigonal coordination. Consequently, TADF properties should also be expected in this case. In the FC region, the lowest excited singlet and triplet states emerge from an LLCT excitation with large contributions from an MLCT($d_{xz}$) configuration as may be clearly seen from the difference density of the $S_1$ state plotted in Fig. 11 (left). The singlet and triplet MLCT($d_{z^2}$) states (Fig. 11, right) only have marginally higher excitation energies at the ground state geometry. The $S_0 \rightarrow S_1$ and $S_0 \rightarrow S_3$ transitions both contribute to the excitation spectrum and should result in emission. With vertical singlet–triplet energy gaps of $\Delta E_{ST} \approx 807\ cm^{-1}$ (0.1 eV), $S_1$ and $S_3$ appear predestined for TADF, provided that their electronic structures and energy splittings do not change dramatically upon geometry relaxation. An overview over the energetic positions of the electronic states at various minimum geometries is provided in Fig. 12.

 

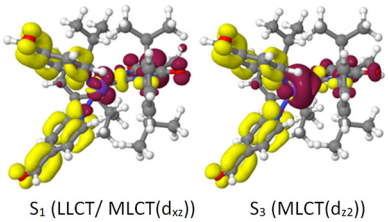


Fig. 11 Difference densities (isovalues ±0.002) of the $S_1$ (LLCT/MLCT($d_{xz}$)) and $S_3$ (MLCT($d_{z^2}$)) states of 3b at the optimized $S_0$ geometry. Red colour signals electron loss, yellow colour electron gain with respect to the electronic ground state density.

The absorption maximum predicted by theory of compound **3b** is at 405 nm and is related to the $S_3 \leftarrow S_0$ transition (Fig. 12). The respective $S_1 \leftarrow S_0$ transition is only observable as a shoulder (excitation spectrum) or weak band (absorbance spectrum) (Fig. 13B). However, the measured absorption and excitation spectra in cyclohexane are blue-shifted compared to the theoretically predicted spectrum (Fig. 13B). The normalized excitation/absorbance ratio at shorter wavelengths indicates the presence of additional non-luminescent species in suspensions (Fig. 13).

The emission spectra in cyclohexane and powder overlap completely (Fig. 13A). The maximum in the steady-state emission spectrum shows a blue-shift from 613 nm at 100 K to 599 nm at 270 K (Fig. 14A), which allows to estimate a value of $\Delta E_{ST}$ = 381 $cm^{-1}$ (47 meV). At temperatures below 100 K, the maximum does not show any additional shift, but an additional band is observed. This band is assigned to luminescence of leached free ligand 4-formyl pyridine (Fig. 14B), which was dissociated from the surface of the microcrystals before freezing. Another confirmation of this interpretation is the absence of this band in the respective solid-state measurements, indicating that this process only occurs with measurable significance in suspension. Concerning the chemical stability of this compound, this is an expected observation, since complex **3b** proved to be the least stable of the four investigated compounds.[43]

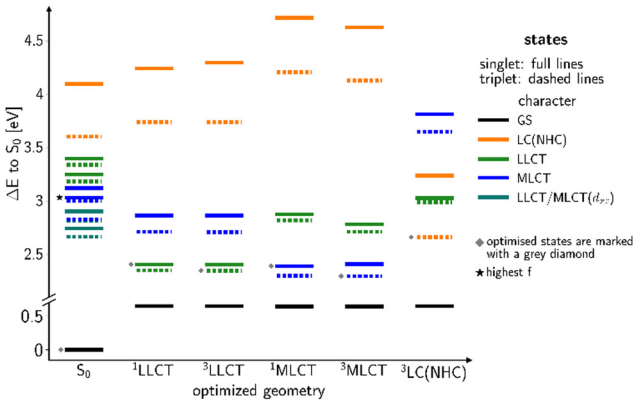


Fig. 12 Overview over the computed vertical DFT/MRCI energy levels at optimized geometries of low-lying states of complex **3b**. The $S_0$ energy at the optimized ground-state geometry serves as common energy offset.

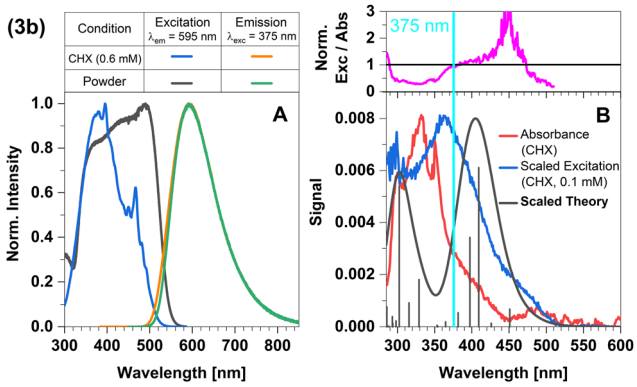


Fig. 13 Spectra of compound **3b** at 298 K (summary in Table 1). The measurements procedures are described in detail in Experimental and theoretical procedures. (A) Excitation and emission spectra in liquid cyclohexane (CHX) and powder. (B) For a qualitative comparison of the absorption properties, the excitation and the broadened DFT/MRCI spectrum were scaled to the experimental absorbance spectrum, which was corrected for baseline and scattering (eqn (3)).

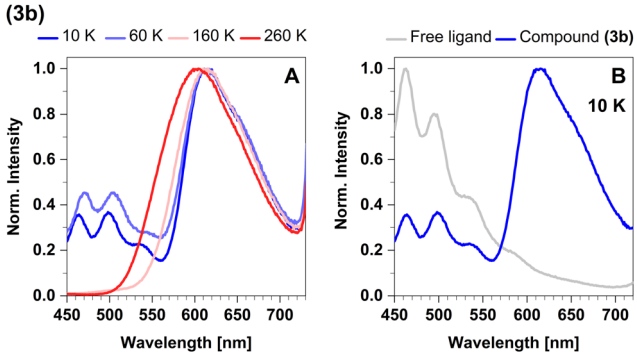


Fig. 14 (A) Steady-state luminescence spectra of **3b** in cyclohexane suspension at selected temperatures of 10 K, 60 K, 160 K, and 260 K. (B) Comparison of the steady-state spectrum of **3b** with the spectrum of the free ligand (4-formyl pyridine) obtained in cyclohexane solution at 10 K. The excitation wavelength was 375 nm.

The energetic proximity of MLCT($d_{z^2}$) and MLCT($d_{xz}$) states promises enhanced SOC. According to El-Sayed's rule,[44] the rate of ISC is relatively large if the non-radiative transition involves a change of orbital type. Although this rule was originally formulated for heterocyclic organic compounds, it can be extended to include transition metal complexes as well.[14] This extended version states that fast ISC is expected if the states are singly excited with respect to each other, the local orbital angular momentum $l$ is conserved and the magnetic quantum number $m_l$ changes by 0, ±1 unless $m_l$ = 0 where $\Delta m_l$ = ±1 is required. In the present context of **3b**, this means that strong SOC is expected between MLCT($d_{z^2}$) and MLCT($d_{xz}$) or MLCT($d_{yz}$) configurations with a common ligand acceptor orbital. The large calculated rate constants for the ISC and rISC transitions between these pairs of states (Fig. 15) suggest that their populations fully equilibrate at room temperature at higher rates than radiative decay, which, in turn, appears to be the rate-determining step (microseconds) in this complex.

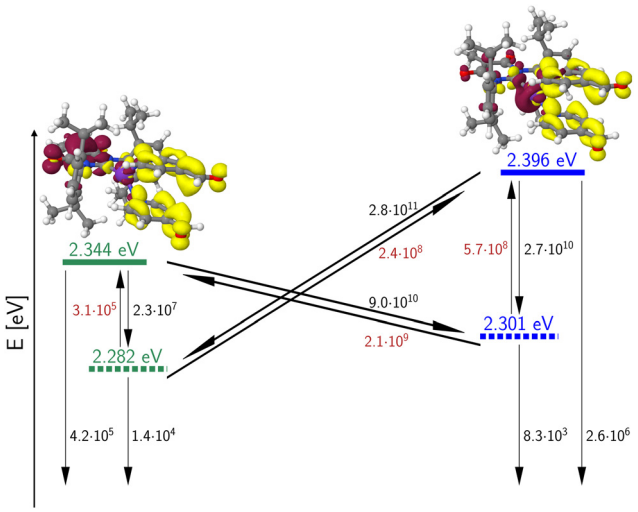


Fig. 15 Calculated 0–0 energies of the LLCT/MLCT($d_{xz}$) (green) and MLCT($d_{z^2}$) (blue) states of **3b**. Singlet states are symbolized by solid line, triplet states by dashed lines. ISC and rISC rate constants [$s^{-1}$] were determined in Condon approximation for a temperature of 298 K. Rate constants of thermally activated processes are given in red. The fluorescence and phosphorescence rate constants [$s^{-1}$] were computed according to the Einstein formula and do not include FC factors. The insets depict difference densities (isovalues ±0.002) of the $^1$LLCT (left) and $^1$MLCT($d_{z^2}$) states at their respective minimum geometries. For colour codes, see Fig. 11.

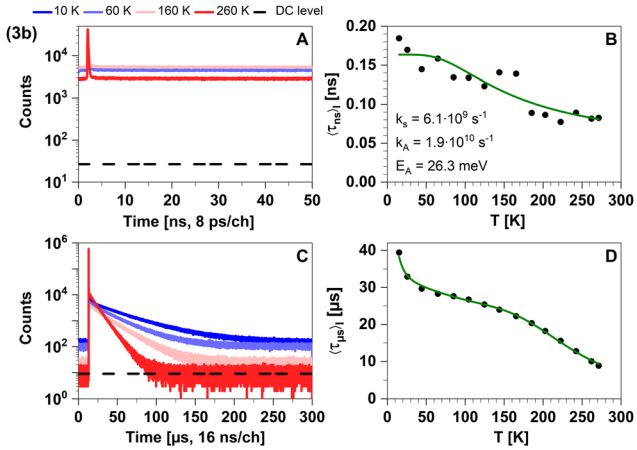


Fig. 16 Time-resolved luminescence measurements of compound **3b** in solid cyclohexane suspension at selected temperatures of 10 K, 60 K, 160 K, 260 K, in two distinct time regimes. Related decay components recorded in the temperature range from 10 K to 270 K are provided in Fig. S5 and S6 (ESI†). The excitation wavelength was at 375 nm, and the detection wavelength 595 nm. (A) Decay curves in nanoseconds. (B) Temperature-dependence of the intensity-weighted prompt fluorescence lifetime $\langle\tau_{ns}\rangle_I$. The green line represents the fit of the experimental data according to eqn (1). All fit results with their respective errors are shown in Table S12 (ESI†). (C) Decays in microseconds. (D) Temperature-dependence of the intensity-weighted luminescence lifetime $\langle\tau_{\mu s}\rangle_I$ with all parameters compiled in Table S16 (ESI†). The green line represents the fit of eqn (2) to the experimental data: $E_1$ to $E_4$ were fixed to the theoretically computed zero-point vibrational energy corrected adiabatic values and $k_0$ to $k_4$ were optimized. The intensity-averaged luminescence lifetimes $\langle\tau_{\mu s}\rangle_I$ are listed in Table 2, the individual decay times and species fractions are compiled in Tables S9–S11 (ESI†). The counts that correspond to the dark count (DC) rate of the detector (95 Hz) are marked with a black dashed line.

We therefore mainly expect delayed fluorescence under these conditions. Indeed, time-resolved spectroscopy measurements show that the prompt fluorescence of **3b** decays at the sub-nanosecond time scale (Fig. 16A), which agrees well with the theoretical predictions. Presumably, a mixture of TADF and phosphorescence is observed in the microsecond time range. This assumption is confirmed by analysis of the temperature dependence of the luminescence decay times (Fig. 16D). Given the El-Sayed allowed ISC process in **3b**, there is also an expectedly strong spin admixture between the $^1$LLCT and $^3$MLCT states, which should lead to radiative decay times in the order of microseconds. This qualitative line of argument proves true considering the values of the computed phosphorescence rate constants of the $^3$LLCT and $^3$MLCT states, which are both of the order of $k_P \approx 10^4$ $s^{-1}$ (Table 3).

This expected time scale is experimentally confirmed. In the microsecond time regime, the decays are characterized by a multi-exponential fit function in the entire temperature range from 10 K to 270 K. The intensity-averaged decay times increases from 8.87 µs at 270 K to almost 40 µs at 10 K (Fig. 16D and Table S11, ESI†). We monitor three characteristic temperature regions: between 270–200 K (Fig. S6A, ESI†), the emission amplitude of delayed emission decreases, which is a characteristic observation for TADF. Between 200–100 K (Fig. S6B, ESI†), this amplitude remains constant. However, upon further cooling (between 100–10 K, Fig. S6C, ESI†), the amplitude rises again, indicating the presence of an alternative process distinct from TADF. The temperature dependence of the corresponding amplitudes and lifetimes is shown in Fig. S7 (ESI†). This observed behaviour is anticipated because the thermal energy is not sufficient to overcome the computed energy gap of $\Delta E_{ST}$ = 62 meV. This value is close to the one derived from the spectral shift observed in the steady-state data (47 meV). Additionally, the observed spectral red-shift in the steady-state emission spectra upon cooling provides further evidence of phosphorescence becoming the dominant emission source at lower temperatures. An important experimental hint for this tightly coupled ensemble of states (red box in Fig. 17) is the fit of the microsecond time domain temperature-dependent decay times to eqn (2). Using the theoretically predicted energy gaps between the relevant $^1$LLCT, $^3$LLCT, $^1$MLCT, and $^3$MLCT states of **3b** and optimizing the five corresponding rate constants, the agreement between theory and experiment is striking. Notably, the fitted rate constants are close to the theoretically predicted values (Table S16, ESI†).

Due to the high MLCT contributions to their electronic wavefunctions, the $T_1$ states exhibit large SOCMEs with several excited singlet states with high oscillator strengths from which the spin-forbidden transitions borrow intensity. The calculated spin-component averaged phosphorescence rate constants are of the order of $k_P \approx 10^4$ $s^{-1}$. Considering that only a small portion of the excited molecules radiatively decays ($\Phi_{PL}$ = 0.13 was measured in the solid state at room temperature,[43]), these kinetic constants are consistent with the measured decay times

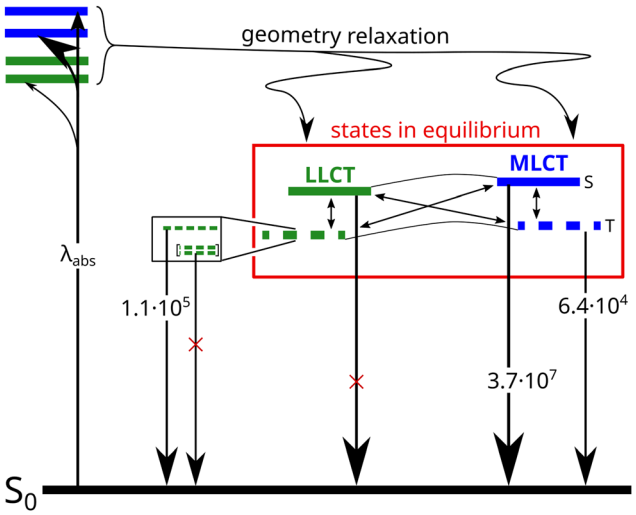


Fig. 17 Kinetic scheme of the photo excitation decay of **3b**. The rate constants of the radiative transitions were obtained by fitting the temperature-dependent decay times to eqn (2) using fixed theoretical energy separations. Solid horizontal lines indicate singlet states, dashed lines triplet states. The zero-field splittings of the triplet sublevels are not drawn to scale.

of roughly 10–40 μs (Table S10, ESI†) for the slow component. All-in-all, complex **3b** appears to be a promising starting point to synthesize derivatives with a more stable and rigid structure for harvesting singlet as well as triplet excitons in an OLED. In the solid state, it emits orange luminescence with a absolute photoluminescence quantum yield of $\Phi_{PL}$ = 0.13, which is approximately 3 to 10 times higher than for the other three studied complexes. In suspensions, we could measure only normalized photoluminescence quantum yields $\Phi_{PL}^{norm}$ (see Table 1), which were computed by normalization of the respective signals to the signal of compound **3b**. $\Phi_{PL}^{norm}$ allows us to quantify the photoluminescence yield of **3b** with respect to the other complexes. In suspensions, the increase of the photoluminescence yield for **3b** is more pronounced (12 to 100 times, Table 1). It should be noted, however, that **3b** is chemically labile in solution unless 4-formylpyridine is added in excess. Thus, decomposition products might have slightly affected the determination of the normalized photoluminescence quantum yields in Table 1. Obviously, the formyl substituent in *para* position does not only increase the π-acceptor strength, it also reduces the σ-donor strength of the pyridine ligand. Thus, work is underway to synthesize trigonal complexes with two π-accepting ligands tethered together, which should enhance their chemical stability.

## Summary and conclusions

The aim of this work was the design of electrically neutral linear or trigonal TADF emitting Cu(I) complexes with a strongly σ-donating anionic carbene ligand and one or two electron accepting ligands to enable thin-film processing of the emitter in OLED technologies. For this purpose, we have combined temperature-dependent time-resolved photoluminescence spectroscopy with DFT/MRCI calculations to shed light on the expected optical performance of a number of selected neutral Cu(I) complexes with pyridine-based acceptor ligands. They are easily accessible in large scales from a coordination polymer intermediate in a straightforward synthetic approach. All investigated complexes show luminescence in the visible range. A clear design pattern towards TADF properties can be extracted from our combined study. If the σ-donating carbene is combined with electron-rich pyridine-derived ligands, carbene ligand-centered states form the first excited singlet and triplet states with a substantial S–T energy gap, which rather leads to the observation of dominantly decoupled prompt fluorescence and phosphorescence (compounds **2a** and **3a**). In contrast, electron-poorer pyridine ligands in such a Cu(I) complex lead to an energetic stabilization of LLCT and MLCT states. The stabilization poses a leverage towards TADF (Fig. 18B and D) as

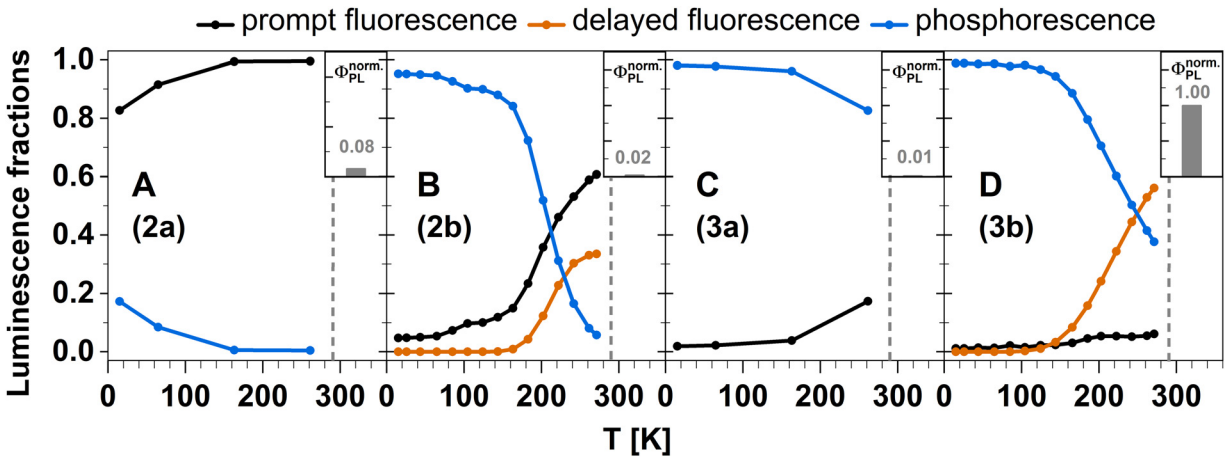


Fig. 18 Temperature-dependent fractions of prompt (black), delayed (orange) fluorescence, and phosphorescence (blue) in the investigated Cu(I) complexes derived by integration of the nanosecond range decay curves and, for **2b** and **3b**, the fitting results of the delayed luminescence according to eqn (2). The insets depict the relative photoluminescence quantum yields of the Cu(I) carbene complexes normalized to the brightest complex **3b**. For details, see Experimental and theoretical procedures.

observed in compounds **2b** and **3b**. In general, trigonal coordination strongly favours ISC and red shifts the emission band compared to the linearly coordinated analogue. With electron-poor pyridine ligands, trigonal coordination also greatly enhances the photoluminescence quantum yield but in the same instance, weakens the Cu–ligand bonds, which reduces the kinetic stability of such complexes in solution.

This sets a general limitation to the photoluminescence quantum yields. One strategy to circumvent this fundamental dilemma is to tether two π-accepting ligands together leading to a trigonal complex with enhanced chemical stability due to the chelate effect. Experiments in that direction are currently pursued in our laboratory. Overall, the present studies offer a detailed overview of the possibilities of targeted molecular design to selectively address desirable optical properties in organometallic compounds.

## Experimental and theoretical procedures

### Materials

**Synthesis and characterization of the compounds.** The complexes were prepared and characterized as described in our preceding publication.[43] In short, the coordination polymer **[An6DAC·Cu]*n*** was obtained by treating an acetonitrile solution of the literature known Li[An6DAC–Cu–Cl] complex[45] with water. Subsequently, this polymer was reacted with an excess of the desired ligands in dichloromethane solution. Removing the solvent *in vacuo* and washing of the residue with diethyl ether yielded the desired compounds **2a**, **2b**, **3a** and **3b**.

### Spectroscopy

**Absorption spectra.** Absorption spectra were recorded on a Cary 4000 UV-Vis spectrophotometer (Agilent Technologies, USA). To minimize artefacts, absorption spectra were measured for diluted samples. Samples were prepared by suspending 0.24 mg, 0.28 mg, 0.17 mg, and 0.22 mg of compounds **2a**, **2b**, **3a** and **3b**, respectively, in a total volume of 3.0 ml of cyclohexane (HiPerSolv Chromanorm for HPLC, VWR Chemicals). The samples were treated in an ultrasonic bath before the measurement. Constant stirring of the suspension during the measurement was achieved by Hellma cuv-o-stirr model 333. The spectrum of each compound was measured five times and averaged. The measured data were corrected for the baseline drifts and strong scattering of the suspensions at short wavelengths. To this end a correction function $A_{\mathrm{corr}}$ was generated and subtracted from the measured spectra. The baseline drift as observed in the absorption-free region of the spectrum ($>550$ nm) was approximated by a straight line. To model the scattering of the suspension of particles with a broad size distribution, a combination of Rayleigh and Mie-scattering was assumed. We used the approximation of Graaff *et al.*[46] where a scattering intensity proportional to $\nu^{0.37}$ was found for particles with diameter $d > \lambda$. Scattering of smaller particles we described with the well-known $\nu^4$ dependence [eqn (3)]:

$$A_{\mathrm{corr}} = a + b\lambda + c/\lambda^4 + d/\lambda^{0.37} \quad (3)$$

with free parameters $a - d$ to be optimized for the respective spectrum. Notably, corrections did not remove or add new peaks (see comparison between raw and corrected data in Fig. S1, ESI†).

Due to partial dissociation of the ligands, the spectra of the suspensions contained, to a different degree, contributions by absorption of free ligand. In order to enable proper comparison with excitation spectra this contribution was compensated by subtraction of independently measured corresponding (baseline corrected) absorbance spectra of free ligand in cyclohexane. The respective spectral contribution of free ligand was estimated around 250 nm, where the complexes showed only small absorption. This correction was required for the trigonal complexes **3a** (pyridine) and **3b** (formyl pyridine).

For comparison to experiment in Fig. 2, 4, 7 and 13, DFT/MRCI line spectra were broadened with a Gaussian of 0.175 meV FWHM. Both the excitation spectrum in cyclohexane and the broadened DFT/MRCI line spectra are scaled to the absorbance spectrum for qualitative comparison. The ratio of excitation and absorbance is normalized at 375 nm.

**Excitation spectra.** The excitation and emission spectra were recorded on a Horiba Fluorolog FL3-22 spectrofluorometer equipped with double monochromators and a cooled PMT. The excitation spectra of diluted suspensions were measured in semi-micro cuvettes (Hellma) with a light path of 4 mm. Samples were stirred all the time during the measurements. The measured data were corrected for inner filter effects in the excitation path using the measured absorbance of the samples in the relevant spectral range. Raman scattering of the solvent and in one case (**3b**) the second order diffraction signal of the excitation light was subtracted (see comparison between raw and corrected data in Fig. S2, ESI†).

Normalized photoluminescence quantum yields $\Phi_{\mathrm{PL}}^{\mathrm{norm}}$ of the complexes were determined in liquid cyclohexane suspensions at 298 K. Absorbance was measured on a Cary 4000 UV-Vis spectrophotometer and corrected as described above. The corrected luminescence spectra were recorded on a Horiba Fluorolog FL3-22 spectrofluorometer at an excitation wavelength of 375 nm. The photoluminescence quantum yields were determined as the ratio between the fluorescence integral and the corrected absorbance at 375 nm. Subsequently, the normalized photoluminescence quantum yields were computed by normalization of the respective photoluminescence quantum yields to that of compound **3b**.

**Time-resolved spectroscopy in the solid state.** Excitation and emission spectra on solid samples were acquired on an Edinburgh Instruments FLS1000 spectrofluorometer with a 450 W Xe lamp, double grating Czerny–Turner monochromators in excitation and emission compartment and a thermoelectrically cooled Hamamatsu PMT-980 photomultiplier tube. All spectra were corrected for wavelength-dependent grating efficiency and detector sensitivity, while the excitation spectra were additionally corrected for potentially fluctuating lamp

 

intensity. Luminescence spectra at 80 K were obtained by placing powdered sample into a liquid $N_2$-cooled Linkam THMS600 temperature cell (temperature precision ±0.1 K) that was coupled to the spectrometer with optical fiber bundles. Time-resolved luminescence in the ns range was measured using time-correlated single photon counting (TCSPC) and a pulsed, mode-locked EPL-375 laser diode (Edinburgh instruments, $\lambda_{em}$ = 375 nm, temporal pulse width ~75 ps, wavelength range ~10 nm, incident average laser power < 0.1 mW) with variable repetition rates (20 MHz to 20 kHz) as the excitation source. Measurements in the μs and ms range were performed with single photon multi-channel scaling (MCS) and a pulsed VPL-420 laser diode (Edinburgh instruments, $\lambda_{em}$ = 423.2 nm, variable temporal pulse width (0.1 μ to 1 ms), wavelength range ~10 nm, incident average laser power 70 mW) and variable trigger frequency (0.1 Hz to 5 MHz).

**Time-resolved spectroscopy in cyclohexane suspensions.** Steady-state and time-resolved measurements of cyclohexane suspensions were measured with a fluorescence lifetime and steady-state spectrometer (FT300 with hybrid PMT detector, PicoQuant, Germany) equipped with a custom designed ColdEdge cryostat powered by a Sumitomo CH-204 cold head and HC-4E Helium compressor (Cryoandmore, Germany). Temperatures were regulated by a temperature controller, Model 335 (Lake Shore Cryotronics, USA), using a silicon diode sensor at the cold head. Sample temperatures were measured independently with a second diode (Model 540 group B, Scientific Instruments, USA; accuracy: ±0.5 K) and used for all analyses. All samples were measured in UV Quartz Type 65FL Macro Cryogenic Fluorescence Cuvette with PTFE Stopper with a light path of 10 mm. For the steady-state and time-resolved measurements in the nanosecond time regime, samples were excited with a supercontinuum laser excitation source (EXW-12 with EXTEND-UV spectral extension unit, NKT Photonics, Denmark). An excitation wavelength of 375 nm was set by tuning the frequency doubler. Time-correlated single photon counting (TCSPC) was achieved with HydraHarp 400 electronics (PicoQuant, Germany). The time bin was 8 ps. For the time-resolved measurements in the microsecond and millisecond time ranges, samples were excited with a modulated continuous wave diode laser (Cobolt 375 nm MLD laser, Series 06-01, Hübner Photonics, Germany). A TCSPC and MCS board, Time Harp 260 (PicoQuant, Germany), provided photon counting and timing. Time bins were 16 ns and 32 ns for repetition rates of 3330 Hz and 1670 Hz, respectively, and 4.1 μs for a repetition rate of 10 Hz. Emission was detected under magic angle conditions. In temperature series measurements, detection wavelengths were set to 460 nm, 540 nm, 495 nm, and 595 nm for **2a**, **2b**, **3a**, and **3b**, respectively. Both temperature series and time-resolved emission spectroscopy measurements were conducted with a scripted measurement routine. All emission spectra were subsequently corrected for wavelength-dependent detection efficiencies of the instrument.

**Fitting and analysis of luminescence decays.** The millisecond (ms) decays in cyclohexane of **2a**, **3a** and **2b**, as well as the free ligands of **2b** and **3b**, were analysed using an in-house written Python script applying a multiexponential model (up to six exponents) and a fixed offset, taking into account the independently measured dark-counts of the detector. The instrument response function (IRF) was approximated by a rectangular function of 100 μs width and used in an iterative reconvolution process to minimize $\chi_r^2$. The fit range covered the full range after the excitation pulse. Decay times from the microsecond (μs) experiments were extracted by tail-fitting a biexponential model to the data using a custom-written LabView script. This model included a free offset to account for the fraction of signal decaying in the millisecond time regime or slower. For **3b**, the photon fraction generating this offset was between 0.07 and 3.4%. From the fit results, photon number weighted average decay times were calculated. Here, the slowest component found in the experiments on **2b** ($\tau$ = 50–240 ms, 5–22% of total signal) was excluded as the corresponding state, due to its long lifetime, is unlikely to be sufficiently thermally equilibrated with the other states.

The averaged lifetimes thus derived for compounds **2b** and **3b** each in general consisted of one dominating component, justifying the assumption of approximate thermal equilibrium populations of the corresponding emissive states that were included in the averaging. Thermal equilibrium between multiple emissive states allows analysis of its temperature dependent luminescence lifetimes with well-established models,[47,48] assuming that the individual emission rate constants $k_i$ are temperature independent. The resulting overall decay time under this condition is the inverse weighted sum of the individual emission rates of the contributing states [eqn (4)]:

$$\begin{aligned}\tau(T) &= \sum_{i=0}^{n} g_i \exp\left(-\frac{E_i}{k_B T}\right) \Big/ \sum_{i=0}^{n} g_i k_i \exp\left(-\frac{E_i}{k_B T}\right) \\ &= 1 \Big/ \sum_{i=0}^{n} x_i(T) k_i\end{aligned} \tag{4}$$

Here $g_i$ is the degeneracy of state $i$, and $E_i$ is the energy difference between state $i$ and the lowest excited state.

Adapted to our systems, we used a model for the excited states consisting of two low-lying triplets with two energetically close singlets. To account for the experimentally observed changes in $\tau$ at very low temperatures (indicating correspondingly small involved activation energies), for the lowest triplet state zero-field splitting was included [eqn (2)]. Fits were performed using OriginPro 8.6 (OriginLab Corporation, USA).

Prompt fluorescence as detected on the nanosecond (ns) time scale was analysed by a multiexponential model (up to 4 exponents) and a variable offset. The IRF was measured using scattered light from a Ludox® solution. To extract lifetime parameters, in-house Python scripts (*ChiSurf*[49]) were employed. From the resulting decay times and amplitudes photon-weighted averages have been generated. Their temperature dependence was approximated by a simple exponential process [eqn (1)].

In the context of the model for the millisecond and microsecond decays as discussed above, detection of nanosecond decays can only be possible when thermal equilibration is not fully established on that time scale. For **3b** the measured singlet decay time (0.3–2.7 ns) is at least 10 times (compared to the fitted rate from the model above) or 100 times (compared to theory output) faster and therefore should not significantly affect the thermal equilibrium.

**Luminescence fractions.** The ratio of prompt (within nanoseconds after excitation) arriving photons to the offset in the nanosecond experiments allowed us to determine the fraction of prompt fluorescence in the total emission. Fit results from eqn (2) were then employed to separate the temperature dependent contributions of thermally activated delayed fluorescence and phosphorescence [eqn (5)]:

$$f_i(T) = g_i k_i \exp\left(-\frac{E_i}{k_B T}\right) \Big/ \sum_{i=0}^{n} g_i k_i \exp\left(-\frac{E_i}{k_B T}\right) \qquad (5)$$

The total phosphorescence and delayed fluorescence contributions were then obtained by adding $f_0(T) + f_1(T) + f_2(T)$ and $f_3(T) + f_4(T)$, respectively. For compound **2b**, the slow decay component that was not included in the averaged decay time was added to the fraction of phosphorescence. Due to its small total fraction (in average *ca.* 10%) the effect on the general appearance of the system was minor.

### Theory

**Quantum chemical methods.** For the geometry optimization of the electronically excited singlet states, time-dependent density functional theory (TDDFT), as implemented in Gaussian 16,[50] was used employing the same basis sets, effective core potentials and density functionals as in previous work.[43] For triplets, the Tamm–Dancoff approximation (TDA) was applied. The corresponding analytical second derivatives were used to generate vibrational frequencies and wavefunctions, required for the computation of FC spectra as well as ISC and rISC rate constants. The effect of an electrostatic environment was mimicked by an implicit solvent model (PCM[51,52]). Point charges result from self-consistent reaction field calculations for a relative permittivity 6.97 (**2a**, **2b**) or (8.93 (**3a**, **3b**)). Singlet and triplet excitation energies and wavefunctions were obtained from multireference configuration interaction (MRCI) calculations at the DFT/MRCI level of theory[53–55] utilizing the same technical parameters as in previous work.[43] SOCMEs were computed with Spock[56] employing a spin–orbit effective core potential on Cu[57] and the Breit–Pauli spin–orbit operator in atomic mean-field approximation on all other atoms. Temperature-dependent ISC and rISC rate constants were computed in Condon approximation employing a Fourier transform approach.[58,59] Before numerical integration, the time correlation function was multiplied by a Gaussian damping function. Its width, the time interval and the number of grid point were varied from case to case to reach convergence. The final parameter sets are listed in Table S21 of the ESI.† Fluorescence rate constants were computed according to the Einstein formula for spontaneous emission based on transition dipole moments and energies from DFT/MRCI wavefunctions. The electric transition dipole moments for computing the probabilities of the spin-forbidden radiative transitions were obtained from DFT/multireference spin–orbit configuration interaction (DFT/MRSOCI) calculations using the appropriate Spock modules.[60] The resulting individual phosphorescence rate constants were then thermally averaged over all triplet spin substates.

## Author contributions

Conceptualization: C. M. M. and M. S.; methodology: J. G., D. S., P. S., S. F., R. K., M. S.; validation: J. G., D. S., P. S.; formal analysis: J. G., D. S., P. S., S. F., R. K., M. S.; investigation: J. G., D. S., P. S. M. S; data curation: J. G., D. S., P. S., S. F., R. K.; writing – original draft preparation: J. G., D. S., P. S., C. M. M., M. S.; writing – review and editing: J. G., D. S., P. S., R. K., C. G., C. A. M. S., C. M. M., M. S.; visualization: J. G., D. S., P. S.; project administration: C. G., C. A. M. S., C. M. M., M. S.; funding acquisition: C. G., C. A. M. S., C. M. M., M. S.

## Data availability

The data supporting this article have been included as part of the ESI. Source data generated in this study, which are presented in the main text and ESI, are provided as Source Data Files *via* the Zenodo repository under the accession code **https://doi.org/10.5281/zenodo.11917519**.

## Conflicts of interest

There are no conflicts to declare.

## Acknowledgements

This work has been funded by the Deutsche Forschungsgemeinschaft (DFG, German Research Foundation), project numbers 396890929 (GRK 2482) and MA 1051/21-1. M. S. is grateful to a materials cost allowance of the Fonds der Chemischen Industrie e.V. and financial support by the ''Young College'' of the North Rhine-Westphalian Academy of Sciences, Humanities and the Arts. C. S. is grateful to the Strategic Research Fund (SFF) of the HHU Düsseldorf for financial support to acquire a ColdEdge cryostat.

## Notes and references

1 C. W. Tang and S. A. Vanslyke, *Appl. Phys. Lett.*, 1987, **51**, 913–915.
2 M. A. Baldo, D. F. O'Brien, Y. You, A. Shoustikov, S. Sibley, M. E. Thompson and S. R. Forrest, *Nature*, 1998, **395**, 151–154.
3 H. Uoyama, K. Goushi, K. Shizu, H. Nomura and C. Adachi, *Nature*, 2012, **492**, 234–238.

 

4 H. Nakanotani, T. Higuchi, T. Furukawa, K. Masui, K. Morimoto, M. Numata, H. Tanaka, Y. Sagara, T. Yasuda and C. Adachi, *Nat. Commun.*, 2014, **5**, 4016.
5 G. Hong, X. Gan, C. Leonhardt, Z. Zhang, J. Seibert, J. M. Busch and S. Bräse, *Adv. Mater.*, 2021, **33**, 2005630.
6 C. Adachi and A. S. D. Sandanayaka, *CCS Chem.*, 2020, **2**, 1203–1216.
7 Y. Zhang, J. Lee and S. R. Forrest, *Nat. Commun.*, 2014, **5**, 5008.
8 R. Czerwieniec, M. J. Leitl, H. H. H. Homeier and H. Yersin, *Coord. Chem. Rev.*, 2016, **325**, 2–28.
9 E. Cariati, E. Lucenti, C. Botta, U. Giovanella, D. Marinotto and S. Righetto, *Coord. Chem. Rev.*, 2016, **306**, 566–614.
10 A. Steffen and B. Hupp, in *Comprehensive Coordination Chemistry III*, ed. E. C. Constable, G. Parkin and L. J. Que, Elsevier, 2021, pp. 466–502.
11 P. S. Wagenknecht and P. C. Ford, *Coord. Chem. Rev.*, 2011, **255**, 591–616.
12 A. Liske, L. Wallbaum, T. Hölzel, J. Föller, M. Gernert, B. Hupp, C. Ganter, C. M. Marian and A. Steffen, *Inorg. Chem.*, 2019, **58**, 5433–5445.
13 J. Föller, C. Ganter, A. Steffen and C. M. Marian, *Inorg. Chem.*, 2019, **58**, 5446–5456.
14 C. M. Marian, *Annu. Rev. Phys. Chem.*, 2021, **72**, 617–640.
15 J. P. Zobel, A. M. Wernbacher and L. González, *Angew. Chem., Int. Ed.*, 2023, **62**, e202217620.
16 Z. A. Siddique, Y. Yamamoto, T. Ohno and K. Nozaki, *Inorg. Chem.*, 2003, **42**, 6366–6378.
17 L. Bergmann, G. J. Hedley, T. Baumann, S. Bräse and I. D. W. Samuel, *Sci. Adv.*, 2016, **2**, e1500889.
18 M. Grupe, F. Bäppler, M. Theiß, J. M. Busch, F. Dietrich, D. Volz, M. Gerhards, S. Bräse and R. Diller, *Phys. Chem. Chem. Phys.*, 2020, **22**, 14187–14200.
19 N. Lüdtke, J. Föller and C. M. Marian, *Phys. Chem. Chem. Phys.*, 2020, **22**, 23530–23544.
20 J. Föller, M. Kleinschmidt and C. M. Marian, *Inorg. Chem.*, 2016, **55**, 7508–7516.
21 R. Hamze, S. Shi, S. C. Kapper, D. S. M. Ravinson, L. Estergreen, M. C. Jung, A. C. Tadle, R. Haiges, P. I. Djurovich, J. L. Peltier, R. Jazzar, G. Bertrand, S. E. Bradforth and M. E. Thompson, *J. Am. Chem. Soc.*, 2019, **141**, 8616–8626.
22 R. Hamze, J. L. Peltier, D. Sylvinson, M. Jung, J. Cardenas, R. Haiges, M. Soleilhavoup, R. Jazzar, P. I. Djurovich, G. Bertrand and M. E. Thompson, *Science*, 2019, **363**(6427), 601–606.
23 T. Y. Li, D. S. Muthiah Ravinson, R. Haiges, P. I. Djurovich and M. E. Thompson, *J. Am. Chem. Soc.*, 2020, **142**, 6158–6172.
24 M. J. Leitl, V. A. Krylova, P. I. Djurovich, M. E. Thompson and H. Yersin, *J. Am. Chem. Soc.*, 2014, **136**, 16032–16038.
25 A. S. Romanov, D. Di, L. Yang, J. Fernandez-Cestau, C. R. Becker, C. E. James, B. Zhu, M. Linnolahti, D. Credgington and M. Bochmann, *Chem. Commun.*, 2016, **52**, 6379–6382.
26 R. Hamze, R. Jazzar, M. Soleilhavoup, P. I. Djurovich, G. Bertrand and M. E. Thompson, *Chem. Commun.*, 2017, **53**, 9008–9011.
27 D. Di, A. S. Romanov, L. Yang, J. M. Richter, J. P. H. Rivett, S. Jones, T. H. Thomas, M. A. Jalebi, R. H. Friend, M. Linnolahti, M. Bochmann and D. Credgington, *Science*, 2017, **356**(6334), 159–163.
28 M. Gernert, L. Balles-Wolf, F. Kerner, U. Müller, A. Schmiedel, M. Holzapfel, C. M. Marian, J. Pflaum, C. Lambert and A. Steffen, *J. Am. Chem. Soc.*, 2020, **142**, 8897–8909.
29 R. Hamze, M. Idris, M. R. Daniel Sylvinson, M. Chul Jung, R. Haiges, P. I. Djurovich and M. E. Thompson, *Front. Chem.*, 2020, **8**, 401.
30 S. Shi, M. C. Jung, C. Coburn, A. Tadle, D. M. R. Sylvinson, P. I. Djurovich, S. R. Forrest and M. E. Thompson, *J. Am. Chem. Soc.*, 2019, **141**, 3576–3588.
31 J. Li, L. Wang, Z. Zhao, X. Li, X. Yu, P. Huo, Q. Jin, Z. Liu, Z. Bian and C. Huang, *Angew. Chem.*, 2020, **132**, 8287–8294.
32 A. Ruduss, B. Turovska, S. Belyakov, K. A. Stucere, A. Vembris and K. Traskovskis, *Inorg. Chem.*, 2022, **61**, 2174–2185.
33 J. Föller and C. M. Marian, *J. Phys. Chem. Lett.*, 2017, **8**, 5643–5647.
34 S. Thompson, J. Eng and T. J. Penfold, *J. Chem. Phys.*, 2018, **149**, 014304.
35 C. R. Hall, A. S. Romanov, M. Bochmann and S. R. Meech, *J. Phys. Chem. Lett.*, 2018, **9**, 5873–5876.
36 J. Eng, S. Thompson, H. Goodwin, D. Credgington and T. J. Penfold, *Phys. Chem. Chem. Phys.*, 2020, **22**, 4659–4667.
37 X. F. Song, Z. W. Li, W. K. Chen, Y. J. Gao and G. Cui, *Inorg. Chem.*, 2022, **61**(20), 7673–7681.
38 T. Hölzel, A. Belyaev, M. Terzi, L. Stenzel, M. Gernert, C. M. Marian, A. Steffen and C. Ganter, *Inorg. Chem.*, 2021, **60**, 18529–18543.
39 F. Chotard, A. S. Romanov, D. L. Hughes, M. Linnolahti and M. Bochmann, *Eur. J. Inorg. Chem.*, 2019, 4234–4240.
40 J. Guhl, *Master's thesis*, Heinrich-Heine University, 2022.
41 M. Gernert, U. Müller, M. Haehnel, J. Pflaum and A. Steffen, *Chem. – Eur. J.*, 2017, **23**, 2206–2216.
42 O. Nolden, J. Kremper, W. Haselbach, M. Morshedi, J. Guhl, P. Schmeinck, C. M. Marian, C. Ganter and P. Gilch, *ChemPhotoChem*, 2023, **7**(4), e202200231.
43 P. Schmeinck, D. Sretenović, J. Guhl, R. Kühnemuth, C. A. M. Seidel, C. M. Marian, M. Suta and C. Ganter, *Eur. J. Inorg. Chem.*, 2023, e202300416.
44 M. A. El-Sayed, *J. Chem. Phys.*, 1963, **38**, 2834–2838.
45 V. César, C. Barthes, Y. C. Farré, S. V. Cuisiat, B. Y. Vacher, R. Brousses, N. Lugan and G. Lavigne, *J. Chem. Soc., Dalton Trans.*, 2013, **42**, 7373–7385.
46 R. Graaff, J. G. Aarnoudse, J. R. Zijp, P. M. A. Sloot, F. F. M. de Mul, J. Greve and M. H. Koelink, *Appl. Opt.*, 1992, **31**, 1370–1376.
47 G. D. Hager and G. A. Crosby, *J. Am. Chem. Soc.*, 1975, **97**, 7031–7037.
48 T. Azumi, C. M. O'Donnell and S. P. McGlynn, *J. Chem. Phys.*, 1966, **45**, 2735–2742.
49 T. O. Peulen, O. Opanasyuk and C. A. M. Seidel, *J. Phys. Chem. B*, 2017, **121**, 8211–8241.
50 M. J. Frisch, G. W. Trucks, H. B. Schlegel, G. E. Scuseria, M. A. Robb, J. R. Cheeseman, G. Scalmani, V. Barone, G. A. Petersson, H. Nakatsuji, X. Li, M. Caricato, A. V. Marenich, J. Bloino, B. G. Janesko, R. Gomperts, B. Mennucci,

H. P. Hratchian, J. V. Ortiz, A. F. Izmaylov, J. L. Sonnenberg, D. Williams-Young, F. Ding, F. Lipparini, F. Egidi, J. Goings, B. Peng, A. Petrone, T. Henderson, D. Ranasinghe, V. G. Zakrzewski, J. Gao, N. Rega, G. Zheng, W. Liang, M. Hada, M. Ehara, K. Toyota, R. Fukuda, J. Hasegawa, M. Ishida, T. Nakajima, Y. Honda, O. Kitao, H. Nakai, T. Vreven, K. Throssell, J. A. Montgomery Jr., J. E. Peralta, F. Ogliaro, M. J. Bearpark, J. J. Heyd, E. N. Brothers, K. N. Kudin, V. N. Staroverov, T. A. Keith, R. Kobayashi, J. Normand, K. Raghavachari, A. P. Rendell, J. C. Burant, S. S. Iyengar, J. Tomasi, M. Cossi, J. M. Millam, M. Klene, C. Adamo, R. Cammi, J. W. Ochterski, R. L. Martin, K. Morokuma, O. Farkas, J. B. Foresman and D. J. Fox, *Gaussian 16, Revision A.03*, Gaussian Inc., Wallingford CT, 2016.

51 E. Cancès, B. Mennucci and J. Tomasi, *J. Chem. Phys.*, 1997, **107**, 3032–3041.

52 B. Mennucci, E. Cancès and J. Tomasi, *J. Phys. Chem. B*, 1997, **101**(49), 10506–10517.

53 S. Grimme and M. Waletzke, *J. Chem. Phys.*, 1999, **111**, 5645–5655.

54 C. M. Marian, A. Heil and M. Kleinschmidt, *Wiley Interdiscip. Rev.: Comput. Mol. Sci.*, 2019, **9**, e1394.

55 A. Heil, M. Kleinschmidt and C. M. Marian, *J. Chem. Phys.*, 2018, **149**, 164106.

56 M. Kleinschmidt, J. Tatchen and C. M. Marian, *J. Comput. Chem.*, 2002, **23**, 824–833.

57 D. Figgen, G. Rauhut, M. Dolg and H. Stoll, *Chem. Phys.*, 2005, **311**, 227–244.

58 M. Etinski, J. Tatchen and C. M. Marian, *J. Chem. Phys.*, 2011, **134**, 154105.

59 M. Etinski, J. Tatchen and C. M. Marian, *Phys. Chem. Chem. Phys.*, 2014, **16**, 4740–4751.

60 M. Kleinschmidt, J. Tatchen and C. M. Marian, *J. Chem. Phys.*, 2006, **124**, 124101.

 